J. Fluid Mech. (1983), *vol.* 128, *pp.* 231–246
Printed in Great Britain

Interference between two circular cylinders forming a cross

By M. M. ZDRAVKOVICH
University of Salford, U.K.

(Received 1 March 1982 and in revised form 6 October 1982)

The interference of flow around two circular cylinders forming a cross can be considered as an element of a gauze screen or an offshore structure. The most important feature of the interference was found to be a significant increase of local drag coefficient due to the symmetric formation of secondary flow patterns. The pressure distribution measured around both cylinders at various spanwise stations was distinctly different for the two cylinders in the region of interference. A strong secondary flow was found behind the upstream cylinder and in front of the downstream cylinder. The secondary flow distorted and displaced the separation streamlines on the upstream and downstream cylinders. This has been verified by oil-film flow visualization.

1. Introduction

The interference of two parallel circular cylinders in close proximity has been dealt with by many researchers and reviewed by Zdravkovich (1977). When the axes of two cylinders are perpendicular to one another a complex three-dimensional flow interference takes place.

The structure of the turbulent wake behind two intersecting cylinders was investigated recently by Osaka *et al.* (1983*a*, *b*). The profiles of time-averaged and fluctuating velocity components were measured at a Reynolds number $R = 8 \times 10^3$ over a wide range of downstream stations from $x/D = 3$–594. They found that the decay rate of the centreline defect velocity was considerably slower than that found in either two-dimensional or axisymmetric wakes. Even far downstream, the wake did not behave as a simple combination of two perpendicular two-dimensional wakes.

Subsequent analysis of the balance of turbulent energy production and dissipation (Osaka, Yamada & Nakamura 1983*c*) showed that the diffusion term was different from that of a two-dimensional wake. The secondary currents were caused by eight streamwise vortices which were symmetric with respect to the wake boundaries, that is a pair in each quadrant. The origin of the eight streamwise vortices was not investigated by Osaka *et al.* (1983*c*).

The practical significance of the interference between two cylinders forming a cross can be found in various fields of fluids engineering. For example, off-shore structures consist of a large number of intersecting circular members. Screens formed from interwoven wires are extensively used in wind and water tunnels to reduce turbulence and in the form of biplanar grids as a means to generate isotropic turbulence (Laws & Livesey 1978). The cross formed by two cylinders in the square test section can be considered as an element of the screen where the tunnel walls could be thought of as 'mirrors'.

The present tests were deliberately limited to the cylinder with small aspect ratios coupled with high blockage ratio as found in screens. The object was to examine in detail the local pressure distribution along the span of two circular cylinders forming

a cross. The Reynolds-number range was chosen to be in the upper subcritical range and extended to the precritical range. The variation of local drag coefficient, base pressure, separation and Strouhal number was measured as affected by the Reynolds number, aspect ratio of the cylinders and blockage. The strong secondary flow near the surface of both cylinders was visualized by using the oil-film technique.

2. Experimental arrangement

The wind tunnel used in this experiment was an open-circuit type with a closed test section of 0·45 m × 0·45 m. Two pairs of aluminium cylinders having diameters of 25·4 and 50·8 mm were used for pressure measurements. The aspect ratios L/D of the two pairs of cylinders were 18 and 9 respectively. The cylinders spanned the test section horizontally and vertically in different planes and the point of mutual contact was in the centre of the test section, as shown in figure 1.

The solid blockage ratios were 5·6% and 11·3% respectively for the upstream cylinders. The blockage in the plane of the downstream cylinders was greater owing to the additional wake blockage of the upstream cylinders. The corrections for the combined solid and wake blockage are not known at present, and all the test results were left uncorrected. It will be shown that the extent of the interference region was greater for the upstream cylinder, and consequently the aspect ratio had presumably a stronger effect than the blockage ratio. The effects of the aspect and blockage ratios cannot be separated in the present tests.

The Reynolds-number range covered by the small-diameter pair of cylinders was from $R = 21{\cdot}2 \times 10^3$ to $51{\cdot}2 \times 10^3$ and for the large-diameter cylinders it was from $42{\cdot}7 \times 10^3$ to $107{\cdot}4 \times 10^3$. These Reynolds-number ranges are in the upper subcritical range where the base pressure and drag coefficient are almost constant for a single circular cylinder.

The pressure tappings were drilled at 0°, 65°, 90° and 180°, and the pressure distribution was measured by rotating the circular cylinder in increments of 15°. The three-dimensional pressure variation along the span was measured by displacing the monitored cross-section sidewise relative to the other cylinder. All cylinders protruded through rubber-sealed holes well outside the test section.

The variation of vortex-shedding frequency along the span of the cylinders was measured with a single hot wire and constant-temperature anemometer. The hot wire was traversed across the wake until a smooth periodic signal was observed on the oscilloscope screen. The signal was then passed through a $\frac{1}{3}$ octave spectral analyser to estimate the frequency of the dominating periodicity. The main object was to find the region where the vortex shedding was suppressed, that is where the periodic signal did not exist.

Oil-film flow visualization was performed by spraying the matt-black cylinder surface with a mixture of fluorescent powder in light oil (Squire 1962). The surface-flow photographs were taken in ultraviolet light and the patterns revealed the erosion of powder after about 20 min running time (Ishihara, Kobayashi & Iwanaga 1982).

3. Presupposed flow pattern

The three-dimensional flow pattern around two cylinders forming a cross may be visualized in two perpendicular planes. Figure 1 (*a*) shows the *top view* of the upstream cylinder placed across the flow when the downstream cylinder appears in section. The streamlines passing around the upstream cylinder are forced to converge by the

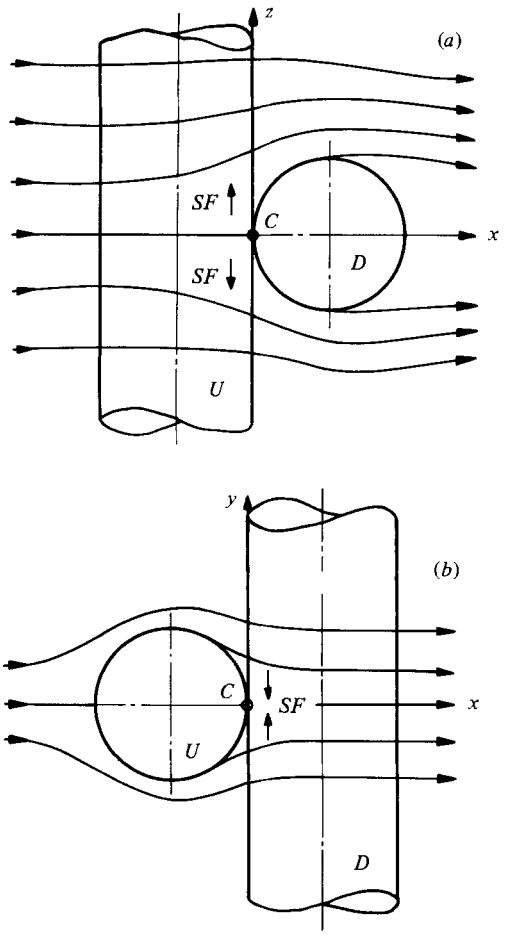

FIGURE 1. Presupposed flow pattern: (*a*) horizontal plane, view from above; (*b*) vertical plane, side view.

downstream cylinder, which acts as an obstacle. The stagnation region and streamlines up to the separation line on the upstream cylinder are only slightly affected by the presence of the downstream cylinder. The presence of the stagnation region in front of the downstream cylinder creates a high local pressure and induces a secondary flow away from the point of contact, as indicated by small arrows in figure 1 (*a*).

Figure 1 (*b*) shows the sideview of the downstream cylinder placed across the flow when the upstream cylinder appears in section. The stagnation pressure along the downstream cylinder becomes gradually reduced as the latter is submerged into the near wake of the upstream cylinder. The pressure difference along the upstream side of the downstream cylinder induces a secondary flow towards the point of contact between the two cylinders.

4. Measured pressure distribution

4.1. *Upstream cylinder*

The strongest interference has been found for the pressure distribution in the plane of contact which was also the plane of symmetry as seen in figure 2. The $C_{p\min}$ was

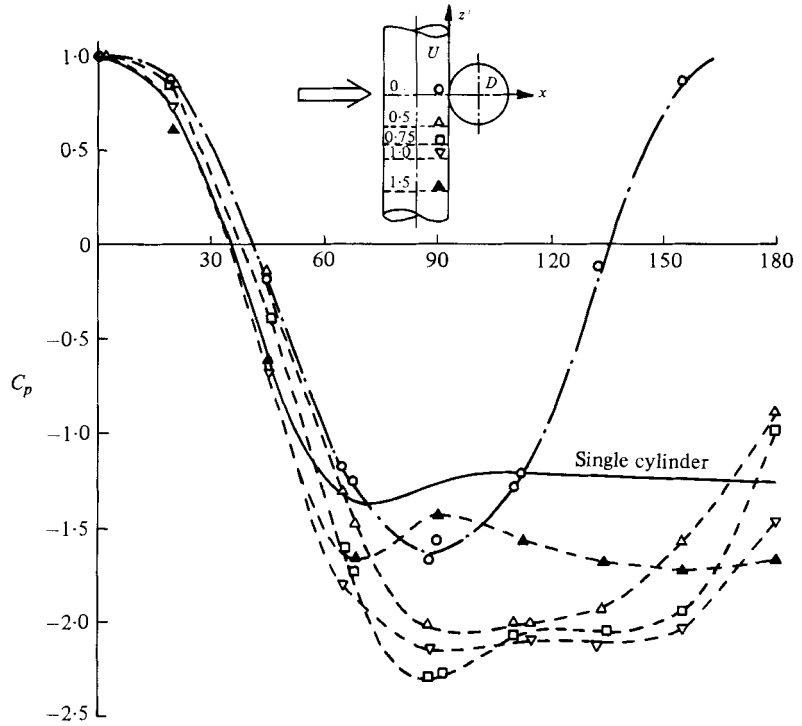

FIGURE 2. Pressure coefficient distribution around upstream cylinder at $R = 42 \times 10^3$.

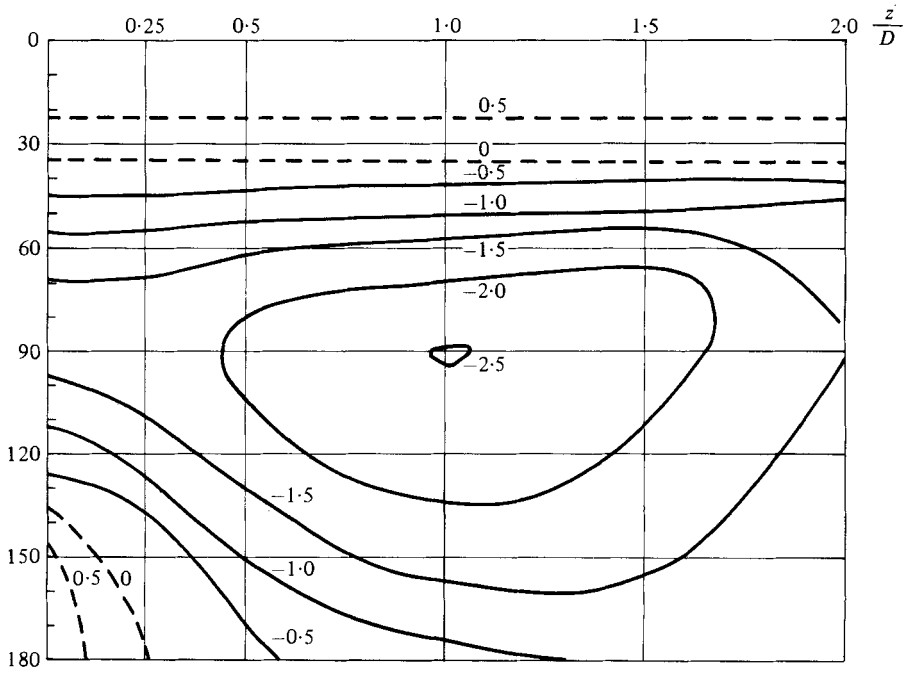

FIGURE 3. Isobars over the surface of upstream cylinder.

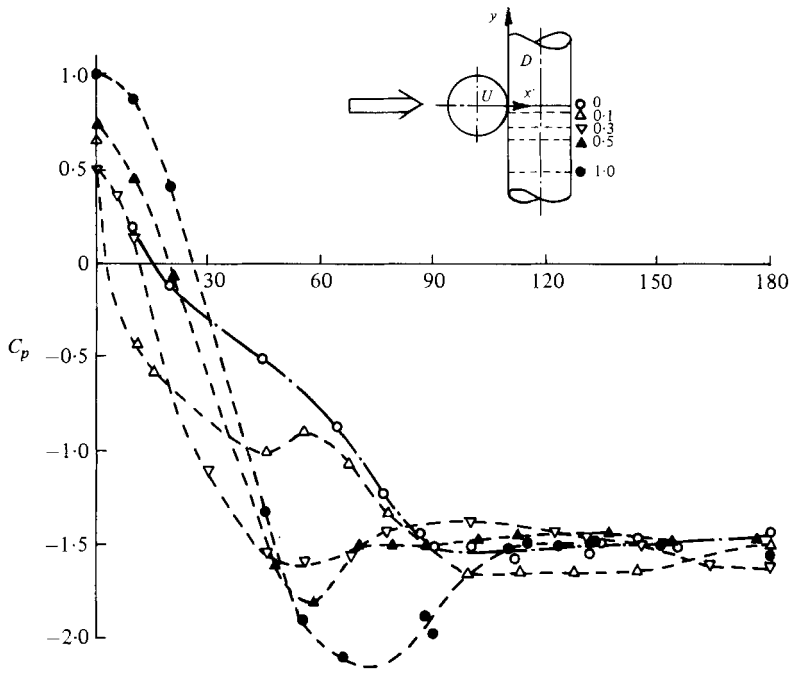

FIGURE 4. Pressure coefficient distribution around downstream cylinder at $R = 42 \times 10^3$.

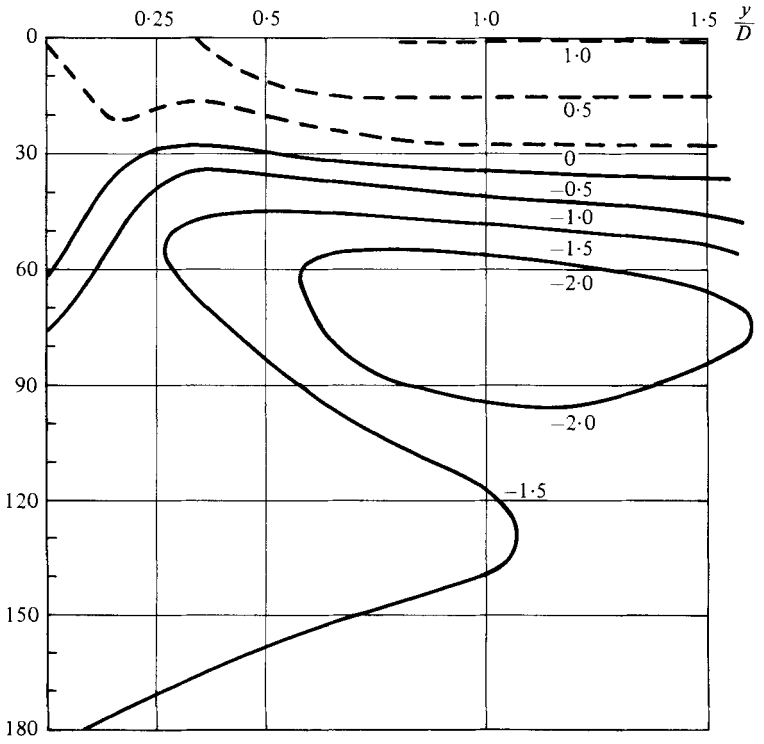

FIGURE 5. Isobars over the surface of downstream cylinder.

reached around 90° but, surprisingly, the pressure recovery continued all the way up to the point of contact. The curve resembled the well-known pressure distribution derived for the potential and irrotational flow around a single circular cylinder.

As the monitored plane was displaced further and further from the contact plane the pressure recovery decreased as well as the value of $C_{p\min}$. The latter reached its lowest value for $|z/D| = 0{\cdot}75$ and then started to increase, as seen in figure 2. The base pressure became flat at $|z/D| = 2$, but the curve was well below that measured for a single cylinder at the same value of $R = 42 \times 10^3$.

The spanwise variation of pressure coefficient and the location of a low-pressure region could also be displayed by plotting isobars on the surface of the cylinder. Figure 3 shows the isobars for 0·5 increments in the pressure coefficient. The front side of the upstream cylinder has no spanwise pressure gradient while the rear side has a considerable gradient capable of inducing a strong secondary flow near the surface.

4.2. *Downstream cylinder*

The pressure distribution curves measured around and along the downstream cylinder are shown in figure 4. Contrary to the wide variation of the base pressure along the upstream cylinder, the base pressure was almost unaffected along the span of the downstream cylinder, while the pressure distribution measured near to the contact plane differed considerably from the rest. The kink and peak at around 60° for $y/D = 0{\cdot}1$ was similar in shape to that found on the downstream cylinder close behind the parallel upstream cylinder (Zdravkovich 1977). The peak in the latter case was attributed to the reattachment of the flow.

Figure 5 shows the isobars over the surface of the downstream cylinder. There is a significant pressure gradient in the vicinity of the point C which can induce deflection of streamlines on the front side of the downstream cylinder, as will be shown by the oil-film visualization.

5. Effect of Reynolds number, aspect and blockage ratios

5.1. *Pressure distribution*

Similar pressure distributions in the corresponding planes were measured at the other Reynolds numbers. The range of Reynolds numbers was extended by using another pair of cylinders twice the size of the initial one. The aspect ratio was reduced from 18 to 9 and the blockage ratio was doubled for the latter.

Figure 6 shows pressure distribution at various spanwise stations for the upstream cylinder at $R = 107 \times 10^3$. The curves are similar to those measured at a lower Reynolds number shown in figure 2. A comparison of figures 2 and 6 reveals that the pressure recovery at 180° in the contact plane is considerably lower at the higher Reynolds number. The second notable difference is in the magnitude of $C_{p\min}$, its spread and very high adverse pressure gradient at $1{\cdot}5D$ from the point C at higher Reynolds number. Regrettably further measurements beyond $1{\cdot}5D$ were not possible with the present length of cylinders.

Figure 7 shows the pressure distribution measured around the downstream cylinder at $R = 107 \times 10^3$. The curves within the range $|y/D| = 0{\cdot}5$ are similar to those found at $R = 42 \times 10^3$. Outside that range, however, there was an increase in magnitude and extent of $C_{p\min}$ – compare figures 7 and 4. The separation could be estimated from the location of the adverse pressure gradient and appeared to be displaced beyond 90°. This indicated that a precritical regime was locally reached.

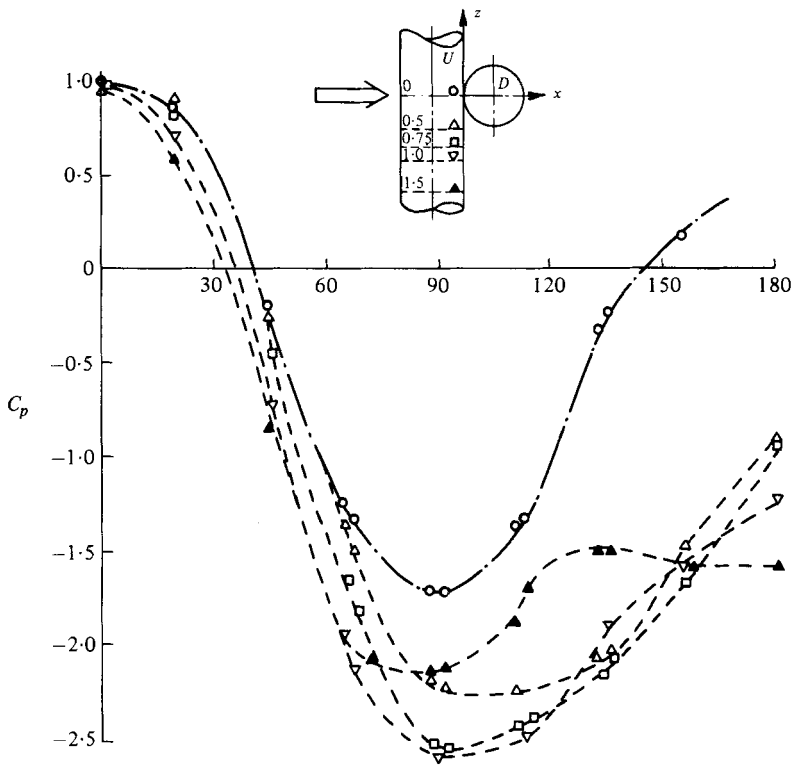

FIGURE 6. Pressure coefficient distribution around upstream cylinder at $R = 107 \times 10^3$.

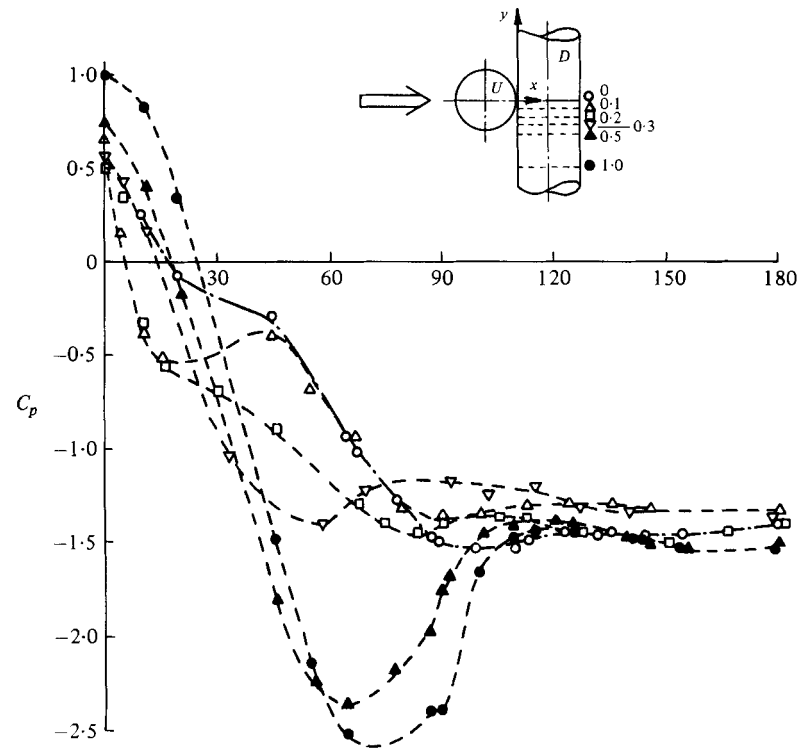

FIGURE 7. Pressure coefficient distribution around downstream cylinder at $R = 107 \times 10^3$.

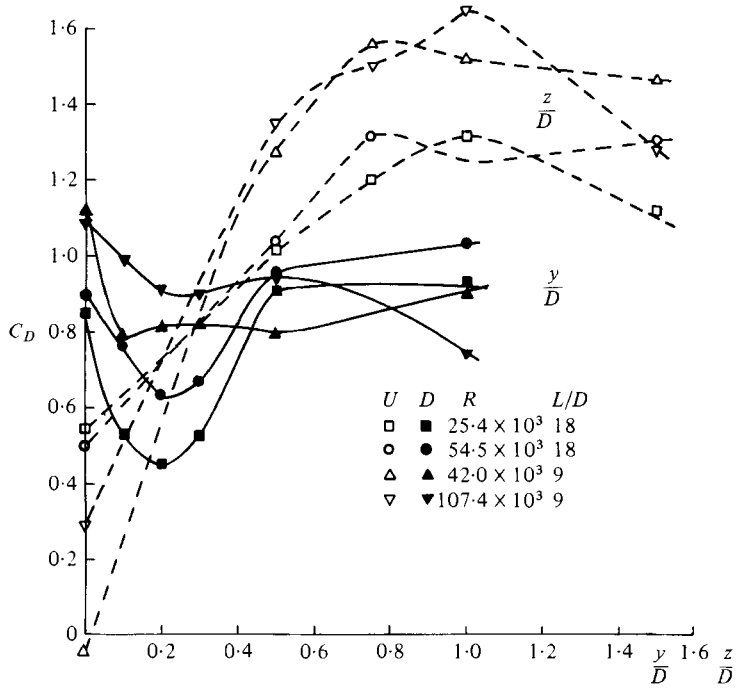

FIGURE 8. Variations of local drag coefficient along the span of crossed cylinders.

5.2. *Local drag coefficient*

The variation of the local drag coefficient along the span of the crossed cylinders was evaluated by integrating local pressure distributions. Figure 8 shows four curves obtained at different Reynolds number for two sets of crossed cylinders. The curves for the same aspect ratio were similar despite the difference in Reynolds number.

The main feature of the variation of local drag coefficient for the upstream cylinder was very low drag in the plane of symmetry C (figure 8). This was followed by a steep rise up to about $|z/D| = 0{\cdot}8$, where the value of local drag coefficient exceeded that found for the single cylinder by 25–30%. The high-drag region persisted up to $|z/D| = 1{\cdot}5$, which was the largest span measured. It would be expected that farther away the local drag coefficient eventually reaches the value found for a single cylinder. The maximum drag coefficient was higher for $L/D = 9$ than for $L/D = 18$, presumably due to the higher blockage. Gould, Raymer & Ponsford (1968) and Okamoto & Yagita (1973) found a similar increase in local drag coefficient near the free end of the single circular cylinder but the rest of the span experienced lower drag than that measured on a nominally two-dimensional cylinder.

The variation of local drag coefficient along the downstream cylinder was considerably less than for the upstream one as seen in figure 8. The pronounced minimum of the local drag coefficient was found only for the higher aspect ratio. The notable decrease of the local drag coefficient from the common trend at $|y/d| = 1$ for $R = 107 \times 10^3$ indicated the precritical regime.

It might be of interest to point out that the interference between two parallel circular cylinders in tandem arrangement showed the opposite trend. The pressure distribution and the pressure drag of the upstream cylinder were almost interference-free, while the downstream cylinder experienced a negative drag for

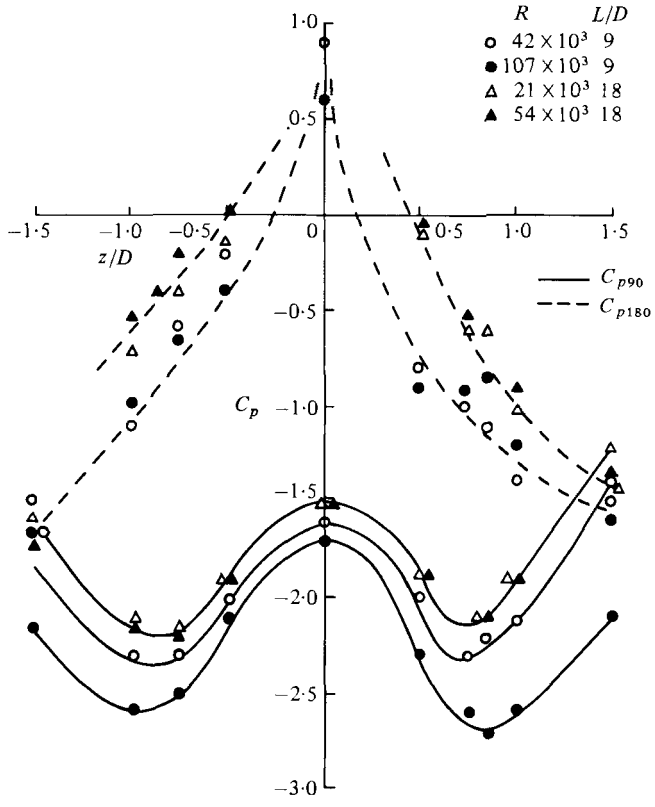

FIGURE 9. Variation of base and side pressure coefficients along upstream cylinder.

small gaps between the tandem cylinders. An entirely different flow pattern in the present case dominated by the secondary flow was the main reason for such a striking dissimilarity. This will be shown in §6.

5.3. *Local stagnation, side and base pressure coefficient*

The strong variation of the local drag coefficients of the upstream cylinder along the span stemmed from an exceptionally steep variation of local base pressure coefficients. Figure 9 shows that the experimental points for the two aspect ratios collapsed into two curves irrespective of the Reynolds number. The magnitude of the pressure gradient along the span was the same in magnitude as the favourable pressure gradient around the front circumference of the cylinder, as can be seen in figure 3. The effect of Reynolds number became noticeable for the C_{p90} curve, particularly for the precritical $R = 107 \times 10^3$, as seen in figure 9.

Figure 10 shows the spanwise pressure distribution along the 0° and 90° lines along the downstream cylinder for various R and L/D. The decrease of C_{p0} towards the plane of symmetry induced a secondary flow, as depicted in figure 1. The effect of L/D was not strong, and tended to reduce the extent of the secondary flow for $|y/D| < 1$ and $L/D = 9$.

A closer inspection of the scatter and unrepeatability of experimental points revealed that sometimes an unsymmetrical flow pattern persisted. Figure 2 shows that for $L/D = 18$ at $R = 21 \times 10^3$ a discontinuous change occurred from low to high values of C_{p0}. This was not investigated further.

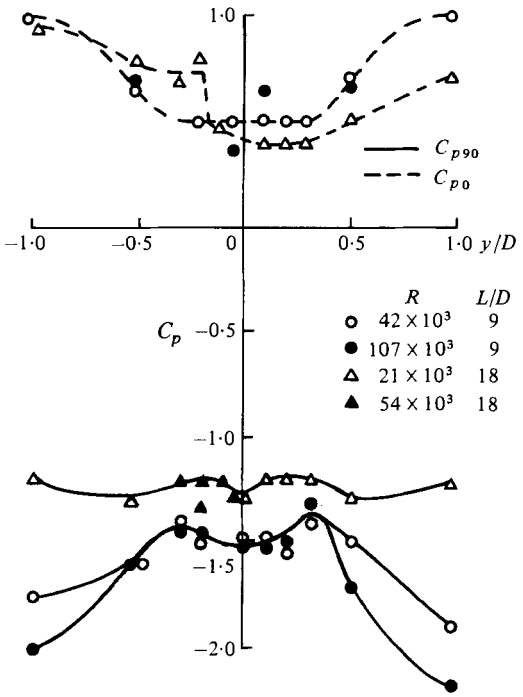

FIGURE 10. Variation of stagnation and side pressure coefficient along span of downstream cylinder.

Finally, the spanwise pressure gradient almost disappeared along the shoulder of the downstream cylinder for $L/D = 18$, as seen in figure 10. It reappeared, however, for $L/D = 9$ with clear branching of the curves for $|y/D| > 0{\cdot}5$ for the higher Reynolds numbers. The significant drop in C_{p90} for $|y/D| = 1$ at $R = 107 \times 10^3$ is another indication of the precritical regime.

6. Surface-flow visualization

Oil-film flow visualization was carried out on the same models at the same Reynolds-number range. The surface-flow pattern revealed not only the separation lines but also the details of the secondary flow in the vicinity of the point of contact of the crossed cylinders.

6.1. *Upstream cylinder*

Figure 11 shows that the separation line was displaced considerably downstream owing to the presence of the downstream cylinder. The separation line formed an arch with distinct 'blobs' of powder dividing the faraway outer regions. The 'blobs' were formed by a vigorous flow behind the separation line predominantly in the spanwise direction. Another strong deflection of the streamlines near the surface is seen in front of the separation line, to the left of the left-hand side blob and partly along the arch itself.

The details of the complex secondary flow near the surface beyond the separation lines could be made visible by moving the camera around the cylinder through an angle of 45°. The archlike separation line appears on the upper half of figure 12, and the contact point C emerges in the middle of the bottom half of the figure. Two

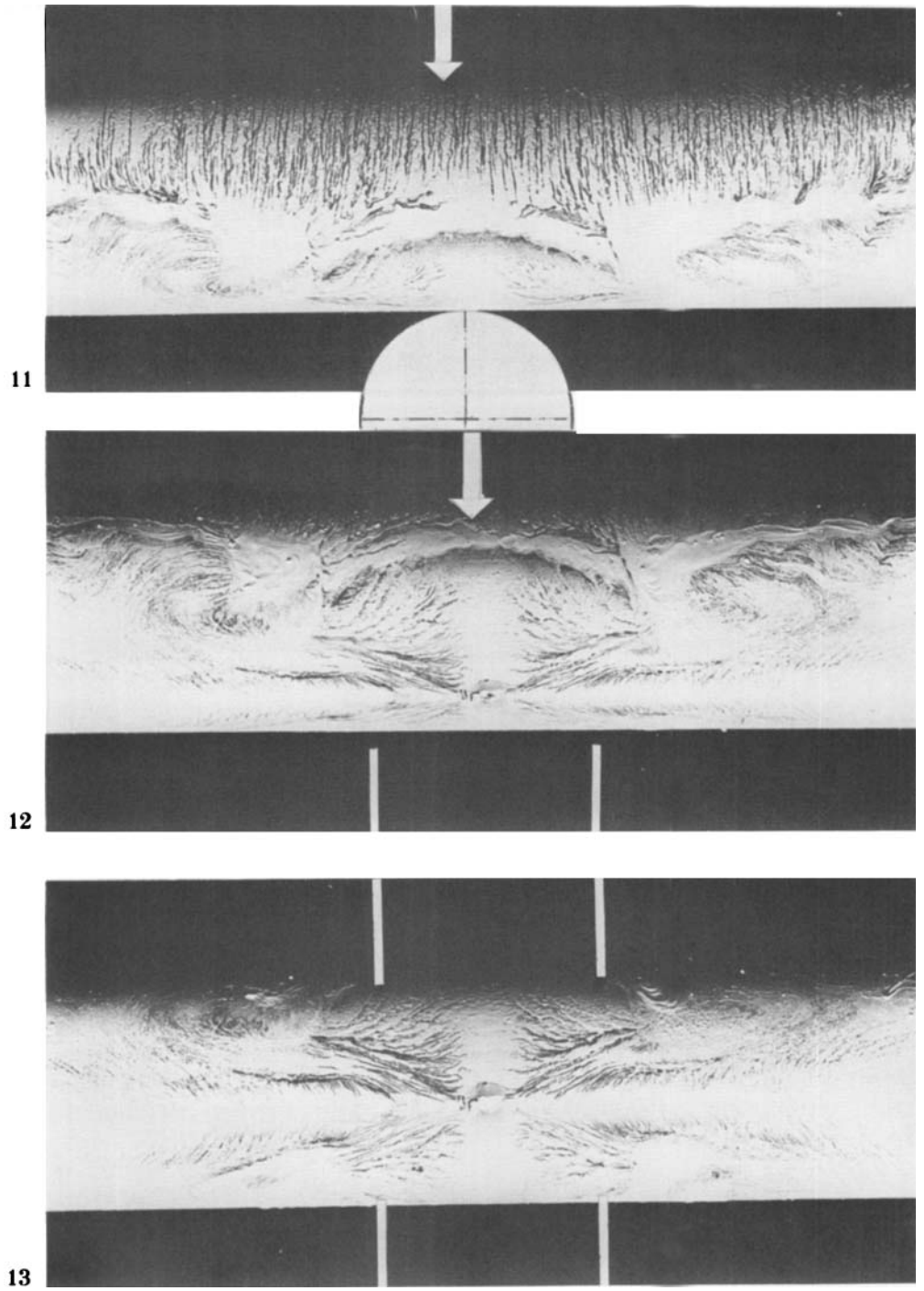

11

12

13

FIGURE 11. Surface flow pattern on upstream cylinder ($L/D = 9$ and $R = 60 \times 10^3$).

FIGURE 12. Same as in figure 11.

FIGURE 13. Same as in figure 12; rear view.

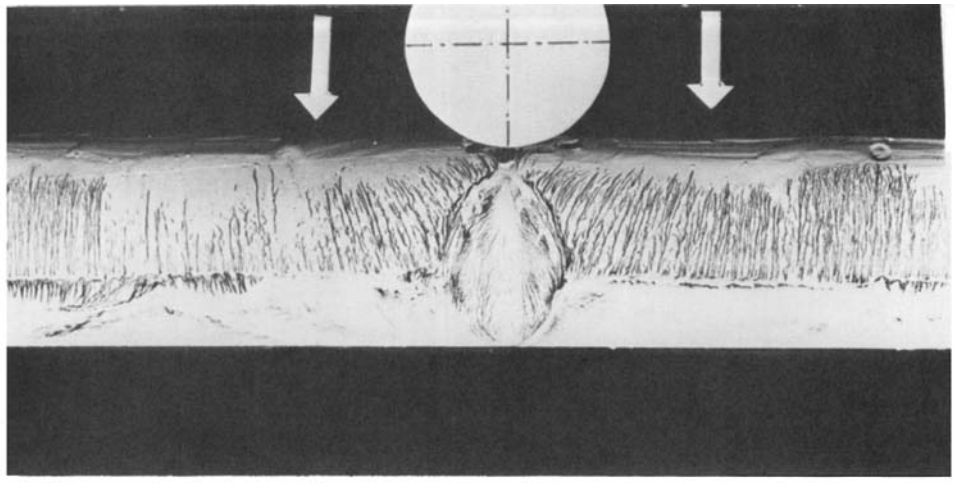

14

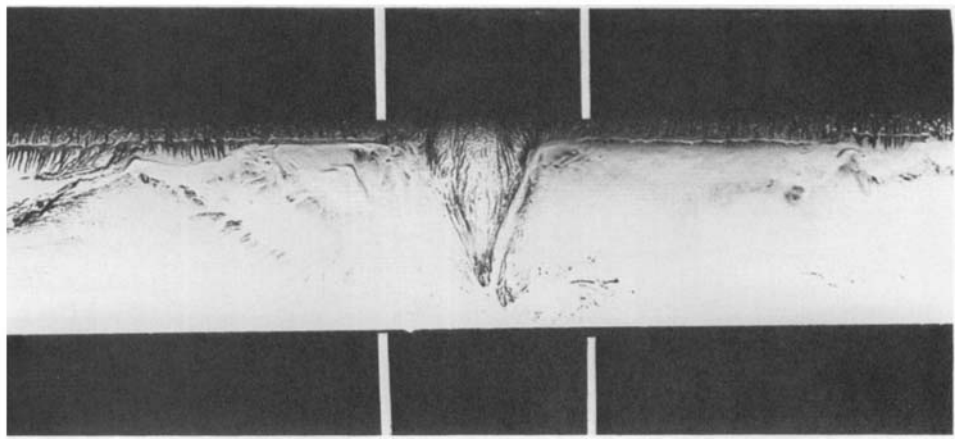

15

FIGURE 14. Surface flow pattern on downstream cylinder ($L/D = 9$ and $R = 60 \times 10^3$).
FIGURE 15. Same as in figure 14; inclined view.

swirling areas about one diameter to the left and right of the plane of symmetry correspond to the low-pressure regions measured on the upstream cylinder and shown in figures 3 and 4.

Further displacement of the camera through another 45° brought the point C to the centre of the photograph in figure 13. The symmetry of the picture is emphasized by the 'herringbone' pattern along the span and by the four swirling regions accompanied by the four blobs.

6.2. *Downstream cylinder*

Figure 14 shows a typical oil-film pattern. The camera was moved around by 15° in order to make the point of contact C visible. All streamlines up to the separation line were deflected towards the plane of symmetry. The separation line, however, was not affected by that deflection and remained distinctly straight† for $|y/D| > 0{\cdot}25$. The

† Slight distortion of the separation line on the left-hand side in figure 14 was caused by an accidental leak of air near the base of the cylinder into the test section. The same could be seen on the left-hand side in figure 15.

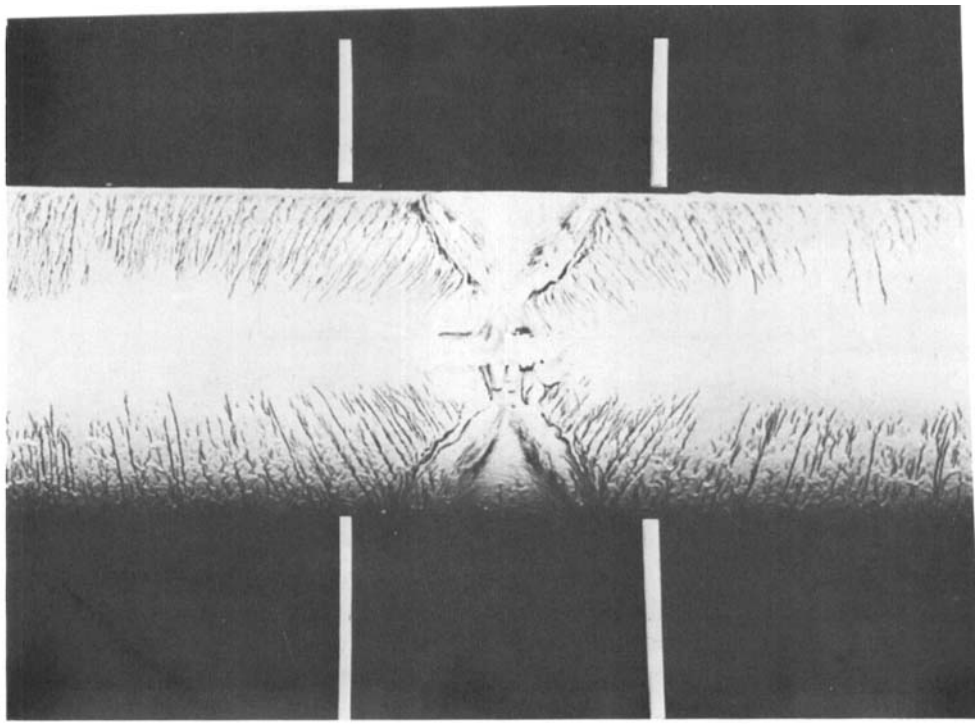

16

FIGURE 16. Same as in figure 15; front view.

separation line was significantly distorted in the narrow region within $|y/D| < 0{\cdot}25$ and had two surprising features.

The first surprise was that the upstream cylinder promoted separation almost from the point of contact at $y/D = 0$. The second surprise was a deep intrusion of the secondary flow along the rear side for $|y/D| < 0{\cdot}25$. Figure 15 shows a distinct V-notch pattern when the camera was moved behind the cylinder and the straight part† of the separation lines appeared along the top half of the photograph. The oil-film pattern runs parallel to the free-stream velocity along the V-notch and turns, near the separation line, parallel to it. Finally, the camera was moved around to show the point of contact in the centre of the photograph in figure 16. The symmetry of the oil-film pattern and front branches of the separation are clearly seen.

7. Interpretation of flow patterns

The bulk of the secondary flow behind the upstream cylinder cannot be visualized by the oil-film technique, which is limited to the time-averaged imprint of the secondary flow in the immediate vicinity of the surface.

The blob produced by the swirling flow in the middle of the low-pressure region on the surface was similar to that observed near the free end of the cylinder by Gould *et al.* (1968). They interpreted it as the foot of a detached longitudinal vortex. Two pairs of such vortices sprang from the sides of the upstream cylinder as sketched in figure 17.

The very early separation from the front side of the downstream cylinder was caused by the rapid 'widening' of the local-flow cross-section between the crossing

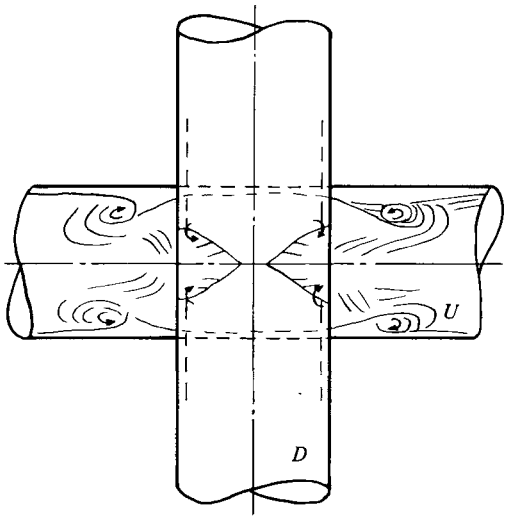

FIGURE 17. Tentative sketch of flow pattern.

cylinders. It can be deduced by referring to figure 1 (*a*) that the streamlines separated from the upstream cylinder were squeezed at first by the front side of the downstream cylinder followed soon by a rapid widening of the local cross-section formed by the cross. This effect vanished beyond $|y/D| > 0{\cdot}25$ from the point of contact C.

The direction of surface streamlines before the separation and secondary flow behind separation corresponded to a swirling flow similar to that found in a horseshoe vortex (Werle 1974). The horseshoe vortex crossed the separation lines at right-angles with small interference as could be seen in figure 14. The velocity induced by the pair of horseshoe vortices kept them attached to the cylinder surface over the rear part of the downstream cylinder. The diffusion of horseshoe vortices required continuous entrainment of fresh fluid which could be supplied only from the secondary flow between them. Hence they gradually approached each other and formed a characteristic V-notch. The deduction is speculative and needs further experimental proof and corroboration.

It is interesting that a mysterious mismatch between two kinds of separation lines observed on the upstream cylinder was similar in shape to that observed by Gould *et al.* (1968) near the free end of the cylinder. The displacement of separation lines towards the rear side was also observed near the ground by Gould *et al.* (1968), Okamoto & Yagita (1973), Etzold & Fiedler (1976) and in these tests during the accidental leak referred to in figures 14 and 15.

8. Vortex shedding along span

Naumann, Morsbach & Kramer (1966) have proposed that an essential requirement for the vortex-shedding process is the straight separation line. The measurement of vortex shedding along the span of both cylinders supported this argument. The frequency of vortex shedding remained constant at all Reynolds numbers despite the strong variation of base pressure along the span of the upstream cylinder. The periodic signal rapidly deteriorated as the location of blobs was approached with the hot wire, and disappeared for all spanwise stations between the blobs. The Strouhal number was between 0·20 and 0·21.

A similar trend was exhibited by the downstream cylinder. The frequency of vortex shedding was periodic and strong up to $|y/D| = 0{\cdot}25$ from the point C. The Strouhal number did not vary along the span, and was about 0·2–0·21. The periodic signal was lost as soon as the hot wire crossed the V-notch region behind the downstream cylinder.

The phase relationship and the interaction of the vortices shed by the cylinders was not measured. Some pertinent results have been reported during the revision of this paper by Donoso, Hillier & Yeung (1982) for two intersecting flat plates.

9. Conclusions

The interference of flow around two circular cylinders forming a cross produced a complicated pattern due to the strong secondary flow. The main features of flow interference can be summarized as follows.

Upstream cylinder

(i) The pressure distribution along the front side was almost unaffected by the downstream cylinder, while that behind the shoulder showed a significant variation culminating in a positive pressure recovery in the symmetry plane towards point of contact C.

(ii) Strong secondary flow along the rear side formed four swirling regions, which were interpreted as detachments of four longitudinal vortices.

(iii) The local drag coefficient was very low in the plane of contact but rapidly increased to 25 % above the value typical for a single cylinder in the subcritical range. The peaks were closely related to the four longitudinal vortices.

(iv) The separation lines were distorted and displaced downstream by the effect of the four longitudinal vortices. The periodic vortex shedding ceased within the region of the four longitudinal vortices.

Downstream cylinder

(i) The pressure distribution along the front side was affected only within $\pm 0{\cdot}5D$ while the base pressure was almost unaffected all along the span. The secondary flow deflected all the streamlines towards the point of contact.

(ii) The point of contact induced an early separation which was interpreted as a horseshoe vortex. The latter crossed the separation lines at right angles and continued attached to the surface in the form of a V-notch.

(iii) The local drag coefficient varied considerably less along the span than for the upstream cylinder.

(iv) The periodic vortex shedding was clearly detectable only behind the straight separation lines. It ceased behind the V-notch region.

The most important finding from the practical point of view was the increase of the local drag coefficient within the interference region. The total drag coefficient will be only slightly affected for the high aspect ratios, but for the small aspect ratios, as found in screens and grids, the local drag increase will have a dominating effect.

The author would like to give credit for the experimental assistance to his former undergraduate students: Q. Iqbal, K. Mehta and C. W. Mock. Professors I. Nakamura and H. Yamada kindly provided early manuscripts of their papers, which will be published in English in 1983.

REFERENCES

DONOSO, J. A., HILLIER, R. & YEUNG, C. K. 1982 The effect of strong three-dimensional disturbance on vortex shedding. In *Proc. 5th Colloquium on Industrial Aerodynamics* (ed. C. Kramer & H. Gerhardt), vol. 2, pp. 109–120.

ETZOLD, F. & FIEDLER, H. 1976 The nearwake structure of a cantilevered cylinder in a cross flow. *Z. Flugwiss.* **24**, 71–82.

GOULD, R. E. F., RAYMER, W. G. & PONSFORD, P. J. 1968 Wind tunnel tests on chimneys of circular cross section at high Reynolds numbers. In *Proc. Wind Effects of Bldgs, Loughborough Univ.* (ed. D. J. Johns, C. Scruton & A. M. Balantyne), paper 10.

ISHIHARA, T., KOBAYASHI, T. & IWANAGA, M. 1982 Visualization of laminar separation by oil film method. In *Proc. Flow Visualization Int. Symp.* (ed. W. Merzkirch), pp. 304–308. Hemisphere.

LAWS, E. M. & LIVESEY, J. L. 1978 Flow through screens. *Ann. Rev. Fluid Mech.* **10**, 247–266.

NAUMANN, A., MORSBACH, M. & KRAMER, C. 1966 The conditions of separation and vortex formation past cylinders. *AGARD Conf. Papers* **4**, 539–574.

OKAMOTO, T. & YAGITA, M. 1973 The experimental investigation on the flow past a circular cylinder of finite length placed normal to the plane surface in a uniform stream. *Bull. Japan Soc. Mech. Engrs* **16**, 805–814.

OSAKA, H., NAKAMURA, I., YAMADA, H., KUWATA, Y. & KAGEYAMA, Y. 1983*a* The structure of turbulent wake behind a cruciform circular cylinder. 1st report: the mean velocity field. *Bull. Japan Soc. Mech. Engrs* **26** (to appear).

OSAKA, H., NAKAMURA, I., YAMADA, H., KUWATA, Y. & KAGEYAMA, Y. 1983*b* The structure of turbulent wake behind a cruciform circular cylinder. 2nd report: the streamwise development of turbulent flow fields. *Bull. Japan Soc. Mech. Engrs* **26** (to appear).

OSAKA, H., YAMADA, H. & NAKAMURA, I. 1983*c* Three-dimensional structure of the turbulent wake behind an intersecting circular cylinder. In *IUTAM Symp. on Three-Dimensional Turbulent Boundary Layers, Berlin, 29–31 March* 1982. Springer.

SQUIRE, L. C. 1962 The motion of a thin oil sheet under the boundary layer on a body. In *AGARD* 70, *Flow Visualisation Using Indicators.*

WERLE, H. 1974 Le tunnel hydrodynamique au service de la recherche aérospatiale. *ONERA Publ.* no. 156.

ZDRAVKOVICH, M. M. 1977 Review of flow interference between two circular cylinders in various arrangements. *Trans. A.S.M.E.* I: *J. Fluids Engng* **99**, 618–633.